# High-Throughput Characterization of Pt Supported on Thin Film Oxide Material Libraries Applied in the Oxygen Reduction Reaction

Dominik Schäfer,[†] Cezarina Mardare,[‡] Alan Savan,[‡] Miguel D. Sanchez,[§,⊥] Bastian Mei,[§] Wei Xia,[§] Martin Muhler,[§] Alfred Ludwig,[‡] and Wolfgang Schuhmann*,[†]

[†]Analytische Chemie—Elektroanalytik & Sensorik, [‡]Institut für Werkstoffe, [§]Laboratory of Industrial Chemistry, Ruhr-Universität Bochum, Universitätsstrasse 150, D-44780 Bochum, Germany

ABSTRACT: Thin film metal oxide material libraries were prepared by sputter deposition of nanoscale Ti/Nb precursor multilayers followed by ex situ oxidation. The metal composition was varied from 6 at.% Nb to 27 at.% Nb. Additionally, thin wedge-type layers of Pt with a nominal thickness gradient from 0 to 5 nm were sputter-deposited on top of the oxides. The materials libraries were characterized with respect to metallic film composition, oxide thickness, phases, electrical conductivity, Pt thickness, and electrochemical activity for the oxygen reduction reaction (ORR). Electrochemical investigations were carried out by cyclic voltammetry using an automated scanning droplet cell. For a nominal Pt thickness >1 nm, no significant dependence of the ORR activity on the Pt thickness or the substrate composition was observed. However, below that critical thickness, a strong decrease of the surface-normalized activity in terms of reduction currents and potentials was observed. For such thin Pt layers, the conductivity of the substrate seems to have a substantial impact on the catalytic activity. Results from X-ray photoelectron spectroscopy (XPS) measurements suggest that the critical Pt thickness coincides with the transition from a continuous Pt film into isolated particles at decreasing nominal Pt thickness. In the case of isolated Pt particles, the activity of Pt decisively depends on its ability to exchange electrons with the oxide layer, and hence, a dependence on the substrate conductivity is rationalized.
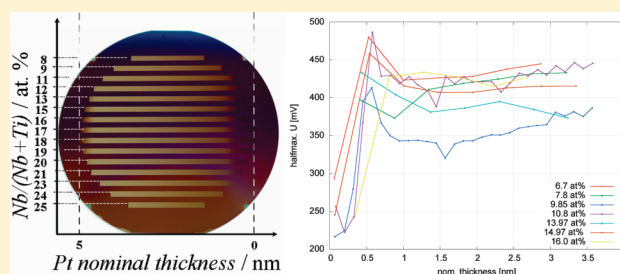
The search for new catalyst/support material systems for high performance oxygen reduction, both concerning activity as well as stability, is extremely difficult due to the huge parameter space (e.g., conductivity, particle size, substrate and catalyst composition, substrate roughness, hydrophilicity, price), which has to be covered for identifying optimized systems. One approach for solving this problem by efficiently screening the parameter space is to adapt combinatorial and high-throughput materials science methods.[1,2] These methods rely frequently on the preparation of thin films by various physical vapor deposition techniques. Materials with a composition gradient on Si wafers, i.e., materials libraries,[2−4] are produced. Materials libraries exhibit an adjustable number of different materials, e.g., a complete ternary system or large parts of quaternary systems, which are obtained in a single experiment under identical conditions and can be screened for the desired properties, thus saving time and energy and gaining a large amount of information as compared with the one-by-one approach.[5,6] Traditionally, optical methods (e.g., fluorescence) are suitable for screening because of their high throughput and were also applied in combination with electrochemical excitation.[7,8] Photoelectrochemical characterization methods irradiate the sample and measure the electrochemical response.[9,10] However, these methods have limitations regarding the amount of information to be gained and are not suitable for all systems, because they expose the whole library to the electrolyte.

For the electrochemical surface characterization of large samples as well as materials libraries, a scanning droplet cell (SDC) has been proposed.[11] A large number of different electrochemical methods can be sequentially applied at preselected spots of the surface.[12] Moreover, the lateral resolution of the SDC can be tuned from millimeters to submicrometers,[13] depending on the precision of the positioning stages, the applied capillary diameter, and the sensitivity of the potentiostat. Meanwhile, the SDC has also been used successfully for screening of materials libaries.[14−16] As another electrochemical method not needing any structured samples, the scanning electrochemical microscopy (SECM) has been applied for catalyst screening using its various modes.[17−22] However, the higher resolution of SECM limits the area that can be screened in practice and increasing the composition gradients to counter this has problems as well (e.g., overlap of diffusion zones).

Titanium oxides with various dopants for ensuring sufficient electrical conductivities are considered as a promising substrate for fuel-cell catalysts due to their price, chemical stability in acidic media, and a potentially positive influence on the activity of the catalyst.[23] While carbon supports exhibit in general problems of substrate oxidation (carbon corrosion)[24] at high anodic potentials,

TiO_2-based supports are expected to be more stable.[25] Because of the photochemical activity of TiO_2, there are as well reports of the use of photogenerated charges to accelerate anodic processes in PEM fuel cells.[26]

In the framework toward reducing the amount of noble metals in fuel cells, it was noted, that very thin layers of Pt have a significantly lower mass-specific activity for oxygen reduction reaction (ORR) than thicker Pt layers.[27] On the other hand, combinatorial investigations on the effect of the Pt thickness and its dependence on the underlying substrate material indicate a possible strategy for circumventing this problem.[28−30] Hayden et al.[30] report findings similar to the ones we will discuss here. However, the applied measuring and evaluation procedures (CO stripping, careful evaluation of Pt oxide reduction) are time-consuming and, hence, only suitable for the used variation of only two different substrate materials. In contrast, we will demonstrate here the preparation of mixed metal oxide material libraries of Ti/Nb by physical vapor deposition and their subsequent spatially resolved, scalable characterization using a SDC as an example to investigate the catalytic ORR activity of thin Pt films on different substrate compositions as well as the dependence of the catalytic activity on the Pt film thickness for a continuous composition spread.

■ FABRICATION AND CHARACTERIZATION OF THIN FILM MATERIAL LIBRARIES

Fabrication of Materials Libraries by Sputter Deposition and Oxidation. The materials libraries were prepared on oxidized 4 in. Si wafers (1.5 μm thermal oxide, 950 °C, wet process) in a two-step process comprising the deposition of metallic (Ti/Nb) precursor layers followed by the oxidation of these precursor layers. Prior to deposition, the targets were presputtered for 5 min. The Ti/Nb precursor multilayers were deposited at room temperature at an Ar pressure of 0.67 Pa by magnetron sputtering in a combinatorial sputter system on unpatterned (S1 and S2) and photolithographically patterned SiO_2/Si wafers (S0).[4] Patterned wafers allow one to accurately determine the thickness of the deposited thin films. The Ti/Nb multilayers were deposited in 45 loops, each loop consisting of a uniform Ti layer of 12 nm thickness (sputter rate 0.32 nm/s) and a wedge-type Nb layer, 1−3 nm film thickness (sputter rate 0.79 nm/s). A moving shutter was used during the Nb depositions to create a thickness gradient across the wafer. By this, the desired composition spread across the wafer is obtained, i.e. 6−27 at.% Nb.

In order to transform the metallic Ti/Nb multilayers to oxides, the materials libraries were heat-treated in air in a furnace at different temperatures (450 °C, 500 °C) and times (2 h, 72 h). Selected samples were additionally annealed in a H_2 flow at 650 °C for 2 h. Finally, Pt stripes (width 3 mm) with a nominal thickness gradient from 0 to 5 nm were sputter-deposited on the oxidized films, with the Pt gradient perpendicular to the concentration gradient in the substrate film in order to obtain material libraries as shown in Figure 1. The highlighted area represents the part from the wafer that was used in the X-ray photoelectron spectroscopy (XPS) investigations. The Nb content across the wafer corresponding to each Pt stripe (numbered from 1 to 15) is indicated at the Y-axis.

Structural and Compositional Characterization of Materials Libraries. The samples were investigated using X-ray diffraction (XRD, PANalytical X'pert Pro, Bragg−Brentano geometry) with Cu Kα radiation in order to identify the phases and to confirm
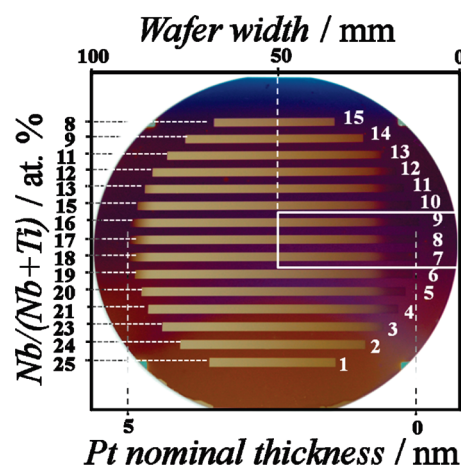
Figure 1. Photograph of a thin film oxide materials library (S1).The Pt stripes are numbered in white (1−15.) On the Y-axis the Nb concentration of each Pt stripe is shown. The gradient of the nominal thickness of the Pt stripes is indicated on the lower X-axis, whereas on the upper X-axis, the width of the wafer is shown. The white rectangle outlines the portion cut from the wafer and the coordinates considered for XPS analysis.

the conversion of the metallic films to oxides. Morphological and compositional characterization was performed using scanning electron microscopy (SEM, LEO) in combination with scanning energy-dispersive X-ray spectroscopy (EDX, Jeol). Thickness measurements were performed using a profilometer (Ambios XP-2) to automatically acquire the thickness values across the wafer. Resistivity measurements were performed using a Keithley 2400 source meter and an automated 4-point probe setup developed in-house and controlled using a LabView program.[31] Metallic materials libraries were oxidized in air, either for 2 h at 450 °C (S1 and stripes from S0) or for 72 h at 500 °C (S2 and stripes from S0). XPS measurements were carried out in an ultrahigh vacuum setup equipped with a Gammadata-Scienta SES 2002 analyzer using a monochromatic Al Kα source (1486.6 eV; 14.5 kV, 45 mA) as incident radiation. The charging effect was compensated using a flood gun. The spectra were taken in a spatial resolution mode using a special slit providing a detection area of 0.015 mm (in the transversal direction) by 1.250 mm (in the longitudinal direction). Due to the sample size restriction of the XPS system, a suitably sized sample was cut from the materials library (see Figure 1), rinsed in high purity acetone, and introduced in the system reaching a base pressure of <5 × 10^{-10} mbar. The survey spectra were taken at 500 eV of pass energy as a function of the positions along the sample. In order to achieve a good signal-to-noise ratio, 20 scans were performed at each position. The analysis was made using CasaXPS version 2.3.15 software using Shirley-type background for peak area quantifications.

Electrochemical Characterization. The basic setup of the droplet cell matches descriptions published earlier[32] with minor layout modifications for reducing its electrolyte volume. The diameter of a pulled borosilicate capillary (~300−400 μm) defines the sample surface in contact with the electrolyte and contains the reference and counter electrodes (250 μm Pt wire), both positioned near the tip of the capillary. The whole cell was mounted to a positioning stage using three stepper motors for moving the cell in the x-, y-, and z-axes. A strain gauge force sensor (2 N full-scale) and a measuring amplifier were used in a

closed feedback loop for reproducibly approaching the tip of the capillary to the surface of the samples with a predefined force. The samples were mounted on a sample holder coated with Teflon for ensuring electrical insulation. The plane of the sample holder can be adjusted by three manual micrometer screws to minimize the tilt angle of the sample with respect to the scanning plane of the capillary.

For scanning droplet cell setups, a miniaturized reference electrode utilizing a pulled glass capillary and an agar gel to solidify the inner electrode[33] is advantageous and often used, because it can be prepared in a compact way and positioned near the working and counter electrodes at the tip of the cell. However, for the current investigations, this electrode type could not be used, because the agar gel quickly liquefied due to the low pH value of the used electrolyte solution. A miniature Ag/AgCl (3 M KCl) reference electrode containing a liquid inner electrolyte was prepared using a borosilicate glass capillary (OD: 1 mm, ID: 0.5 mm), a ceramic frit, and a chloridized Ag wire (∅ 0.25 mm). The commercially available frits initially had a diameter of 1 mm and were polished cylindrically to achieve a diameter of 0.5 mm. These electrodes offer long-term stability for several days of continuous automatic use of the SDC for high-throughput screening. All potentials are measured against this reference electrode.

For measurements without a hanging droplet at the tip of the droplet cell, the tip of the capillary is usually coated with a soft silicone rubber adhesive for achieving a water-tight seal between capillary and sample. The adhesive initially used proved to be insufficiently stable in highly acidic conditions. Finally, Sylgard 184 (Dow Corning) was selected as a compromise between chemical stability, hydrophobicity, and elasticity.

A remote-controlled syringe pump was employed to automatically exchange the electrolyte in the cell after measurements at each scanning grid point. The used electrolyte was flushed into a waste container placed on the sample holder adjacent to the investigated wafer. The volumes of the used vessels for fresh electrolyte and waste are limiting the time span of continuous and unsupervised measurements and allowed about 15 h of screening. Any excess droplets of electrolyte at the tip of the capillary were stripped off by moving the tip to a special position and touching a piece of polishing cloth.

A control software for the whole setup was developed in-house using Visual Basic 6. It allows creating complex sequences of measurements at each point of the scanning grid. It is worth to note that, after droplet cell assembly, initial positioning of sample and cell, contacting of the electrodes, and configuring the scanning grid and experiments, no manual steps are necessary. This allows for a mostly unsupervised screening of suitable samples. The experimental procedure used in this study at each measurement point was designed as follows: (1) Approaching the sample. (2) Recording of various cyclic voltammograms (CVs) for conditioning the sample surface: $0.38\ V \rightarrow 1.4\ V \rightarrow -0.2\ V \rightarrow 0.38\ V$, $v = 0.5\ V/s$ (25 CV); $0.38\ V \rightarrow 0.8\ V \rightarrow -0.2\ V \rightarrow 0.38\ V$, $v = 0.5\ V/s$ (3 CV); $0.38\ V \rightarrow 0.8\ V \rightarrow -0.2\ V \rightarrow 0.38\ V$, $v = 0.1\ V/s$ (5 CV). (3) Recording CVs for evaluating the activity for oxygen reduction: $0.38\ V \rightarrow 0.8\ V \rightarrow -0.2\ V \rightarrow 0.38\ V$, $v = 0.02\ V/s$ (5 CV). (4) Movement to waste position, flushing of electrolyte, and stripping of excess droplets. (5) Movement to the next grid position.

The conditioning serves to clean the Pt surface of adsorbed substances from the environment. Usually, surfaces can be cleaned by polishing prior to measurement, but this cannot be done in case of thin films. Additionally, this procedure aims to achieve comparable surface conditions for different samples.

Chemicals. One molar sulphuric acid p.a. was obtained from Merck (Darmstadt, Germany), and KCl (>99.5%) was from VWR (Darmstadt, Germany). Sylgard 184 was received from Dow Corning (Wiesbaden, Germany); borosilicate glass capillaries were from Hilgenberg (Malsfeld, Germany), and Ag (0.25 mm) and Pt (0.5 mm) wires were delivered by Goodfellow (Bad Nauheim, Germany). All chemicals were used as received.

Data Evaluation Procedures. Since the screening of one of the present materials libraries results in approximately 15 000 CVs, automatic methods for data evaluation and condensation had to be established. Programs in LPC programming language were developed to perform the following tasks: First, each set of CVs was separated into single CVs, and each of them were plotted. An average CV from all the CVs in one set was calculated and plotted as well. All images belonging to one set of CVs were combined into short animated movies to visualize the changes over time. The graphs of the averaged CVs from all measurement points within a line scan were combined into an animation for demonstrating the systematic changes along each of the Pt stripes. After that, specific parameters were extracted from each CV (see below). These parameters and some derived values were tabulated and plotted versus the *x*-coordinate of the measurement point. Thus, different graphs for each line scan were created showing the changes in specific properties along the thickness of the Pt stripe. The combined tabulated data for each wafer was then used to plot a 3D image of several parameters vs substrate composition and nominal thickness. The LPC programs were compiled using LDMud (V3.3.719). All graphs were plotted using Gnuplot (V4.2), and all movies were created by ffmpeg (V3f07f20).

When evaluating only a few measurements, it can be afforded to spend some time on data treatment (e.g., averaging, fitting) and parameter calculation involving human expertise. Additionally, the shape of CVs is usually very similar. In a large number of CVs, this approach is not feasible. We, therefore, concentrated on three parameters, which are easily extracted automatically: the capacitive current (at a potential of 175 mV) indicating the electroactive surface area, an area-normalized oxygen reduction current (at a potential of 350 mV), and the potential at half-maximum oxygen reduction current.

Estimating the active area of a Pt catalyst surface is usually done using either the hydrogen adsorption section of the CV or the CO stripping peaks. For both methods, a specific atmosphere is needed, either CO for the CO stripping method or an oxygen-free environment for achieving a clean hydrogen adsorption without overlaying it with any oxygen reduction. Our screening procedure in the SDC works at ambient atmosphere and cannot alternate between different atmospheric compositions. However, the current in the capacitive section of the Pt CV provides an estimate of the active area and is easily obtained, although it is less precise. The area in absolute units is not calculated, because it depends on the roughness factor of the thin film, which is expected to change along the Pt stripe. Therefore, we normalized the faradaic O_2 reduction currents with the capacitive current for achieving an area-independent dimensionless parameter. The capacitive current was obtained from the last conditioning CV at high scan rates. The O_2 reduction current at 350 mV served as a measure for the catalytic activity for ORR. At this potential, the current is not limited by the mass-transport of oxygen. As stated, also these current values were normalized by the active area.
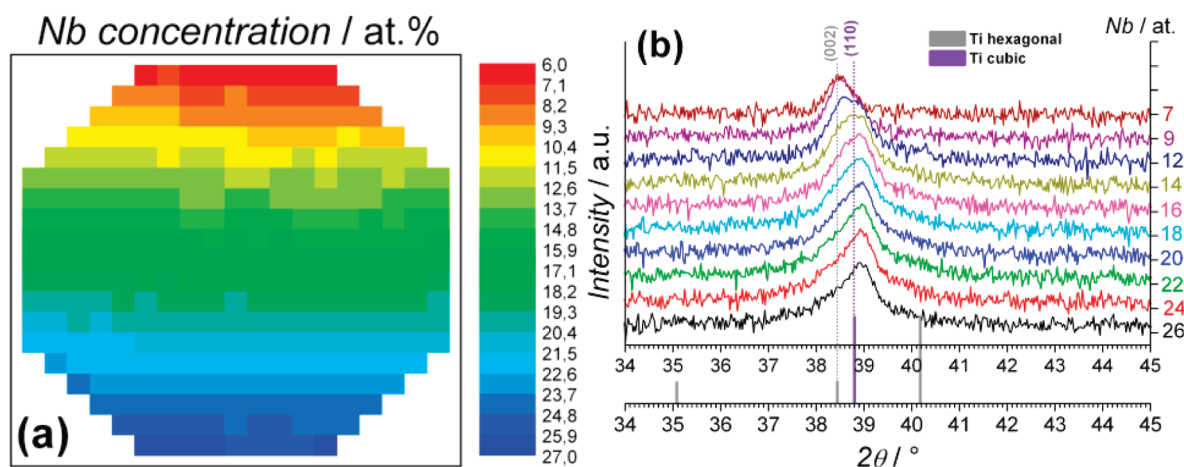
Figure 2. (a) Nb concentration (at.%) map of the materials library S0 showing a Nb gradient from 6 to 27 at%; (b) XRD spectra of the as deposited Ti/Nb thin film materials library S0. The spectra were acquired at different positions across the wafer in order to show the changes of crystallographic phases as a function of the Nb concentration.

Additionally, intrinsically area-independent parameters are the potentials at half-maximum oxygen reduction currents. These maximum currents were obtained at a potential of approximately 100 mV, at which the oxygen reduction is mass-transport limited but not yet superimposed by any hydrogen adsorption or hydrogen evolution. The potentials at 50% of these currents are again in the kinetic section of the CV. Similar to the onset potentials, they were expected to be highly sensitive to any change in the catalytic activity. A catalyst with higher activity will achieve maximum currents at higher potentials than one with a lower activity and thus higher activities lead to a measurable shift in this parameter.

■ RESULTS AND DISCUSSION

Structural and Compositional Characterization. Figure 2a shows the EDX map of the materials library S0 after the Ti/Nb multilayer deposition. The Nb concentration ranges from approximately 27 at.% to 6 at.%, while the Ti concentration changes in the opposite direction from 94 at.% to 73 at.%. The as deposited Ti/Nb thin films have a thickness gradient from approximately 680 to 455 nm. Due to the fabrication method, thickness decreases with decreasing Nb concentration.

Figure 2b shows the XRD patterns of the metallic Ti/Nb thin films as a function of their composition. The phases are changing from the hexagonal Ti [Pauling S456811], which is present up to approximately 10 at.% Nb, to the cubic Ti phase for thin films with higher Nb content (Pauling database S458712). A change from hexagonal to orthorhombic to cubic structures was already reported for Ti samples by increasing the Nb content from 0 to 20 at.% for quenched samples, as well as for alloys prepared by arc melting.[34,35] For the latter, there was a change from hexagonal to orthorhombic at approximately 9.9 at.% Nb and the metastable β-Ti formed at >16.4 at. % Nb.[36] In this work, the orthorhombic phase was not found. Provided that the obtained Ti/Nb films were produced by multilayer deposition at room temperature without diffusion annealing, there are two possible reasons for the peak shifting. On the one hand, it is possible that during sputter deposition of multilayers interdiffusion between Ti and Nb layers occurs: sputtered atoms have relatively high energies, and Ti and Nb have similar atomic radii (140 pm Nb and 146 pm Ti), thus allowing possible interdiffusion. Consequently, the

hexagonal Ti structure is modified into β-Ti. Each Ti layer has approximately 12 nm thickness, whereas the Nb layer is very thin and varies along the wafer from 3 to 1 nm. For sputtered multilayers of Ti and Ni (135 pm atomic radius), it was found that approximately 10% of the layer's thickness was interdiffusing during the sputtering process.[37] On the other hand, the interface between the Ti and Nb layers with the cubic structure of Nb may act as a seed layer for Ti deposition. Consequently, Ti may grow with a cubic structure leading to the presence of β-Ti in the diffraction pattern.

Figure 3 shows the XRD patterns of the Nb–Ti material library S1 oxidized at 450 °C for 2 h in air. For a Nb content below 10 at.%, the detected phases are metallic hexagonal Ti and a Ti-suboxide, Ti_3O (PDF#721806). With increasing Nb content, other diffraction peaks appear, which can be attributed to the intermetallic phase $NbTi_4$ with orthorhombic structure (PDF#170102). No peaks of the TiO_2 rutile phase, which is the most stable titanium oxide phase, were found. The Ti_3O phase is present only in a range of oxygen concentrations from 20 to 30 at.%, as found in the O–Ti phase diagram taken in air at temperatures above 400 °C (Pauling database, C901814). This indicates that the metallic thin film is not fully oxidized, with probably only a very thin layer of TiO_2 being present at the surface, whereas inside the film the oxidation process, which is governed by oxygen diffusion, leads to the formation of only the Ti_3O suboxide and even unoxidized metal remains after 2 h oxidation time at 450 °C. For higher Nb concentrations, the intermetallic phase $NbTi_4$ is formed during the heat treatment via interdiffusion between the Ti and the Nb layers.

After oxidation for 72 h at 500 °C in air, the materials library S1 shows mainly TiO_2 rutile (PDF#782485) and Ti_2O (PDF#721805) phases (Figure 3). The peak at $2\theta = 37.8°$ might belong to the TiO_2 anatase phase, but because the main peak of this phase (25.3°) is missing, it cannot be indentified with certainty. For >24 at.% Nb, the main phase is TiO_2 rutile. The TiO_2 rutile phase changes to the Ti_2O suboxide as the Nb concentration decreases, and it becomes the predominant phase for Nb contents <12 at.% with most probably an outer TiO_2 layer and an inner Ti_2O suboxide.

Figure 3 indicates the existence of a relationship between the Nb concentration and the occurrence of the rutile phase of TiO_2.
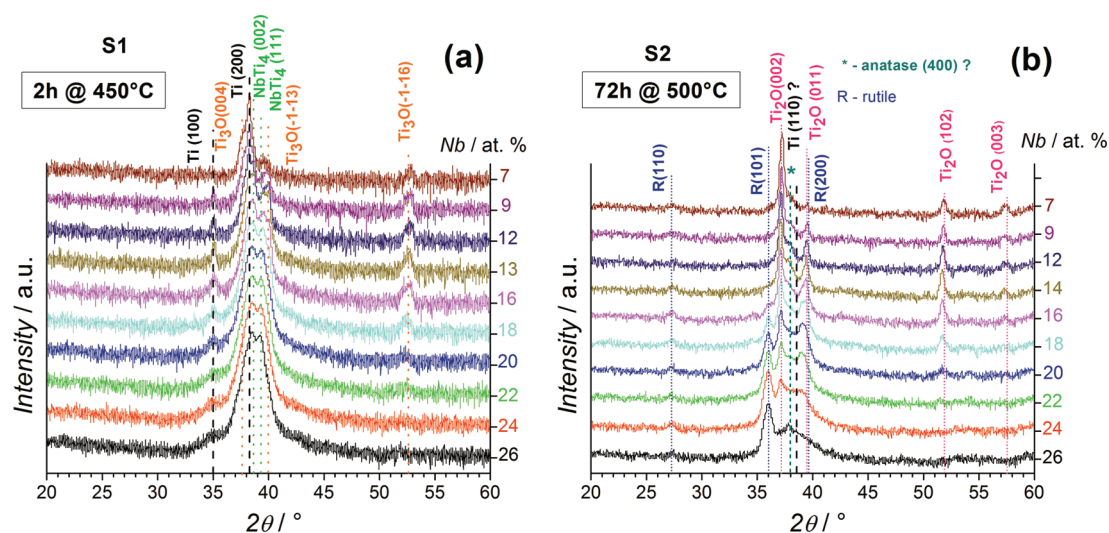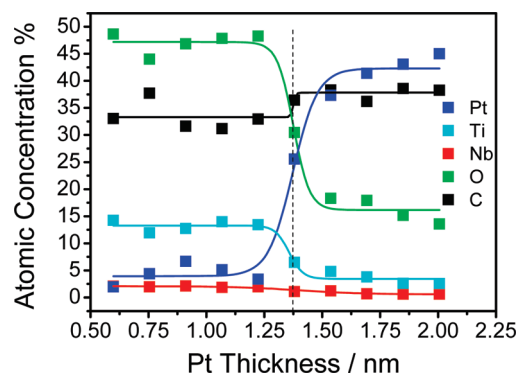
Figure 3. XRD spectra as a function of the Nb concentration for the metallic thin film materials library: (a) S1 after oxidation for 2 h at 450 °C and (b) S2 after oxidation for 72 h at 500 °C.
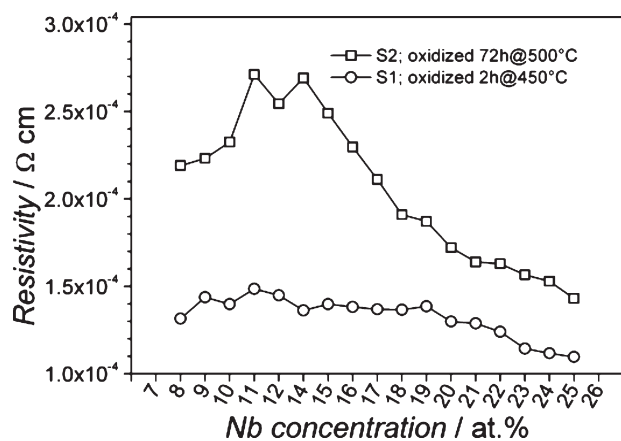
Figure 4. Resistivity as a function of Nb concentration for the materials libraries: (a) S1 after oxidation for 2 h at 450 °C and (b) S2 after oxidation for 72 h at 500 °C.

Figure 5. Atomic concentrations of elements measured by XPS as a function of the nominal Pt thickness.

A possible explanation for the occurrence of rutile is related to the lower oxidation rate observed for Ti–Nb alloys as compared to pure Ti when oxidized at 900 °C in air if no secondary $TiNb_2O_7$ phase was formed.[37] The presence of Nb layers at the metal/gas interface which are oxidized in between the Ti oxide layers or the mixture of Ti–Nb oxides slows down the further oxygen diffusion into the multilayer structure. Consequently, on the one hand, the surface benefits from the higher amounts of oxygen, leading to the formation of the rutile phase of TiO_2. On the other hand, the film is poorly or not at all oxidized close to the metal/substrate interface, as suggested by the absence of Ti_2O suboxide peaks and the broad diffraction peak present at $2\theta = 37–39°$, which is indicating the presence of metallic Ti.

The resistivity values of the oxides of the materials libraries S1 and S2 (Figure 4) are low, approximately 1×10^{-4} Ω cm for S1 and from 1×10^{-4} Ω cm to 3×10^{-4} Ω cm for the materials library S2. These low values are attributed to the presence of Ti suboxides as well as metallic phases. It was already reported that Ti suboxides possess low resistivity values.[38] The materials library S1, being the least oxidized one, shows the lowest
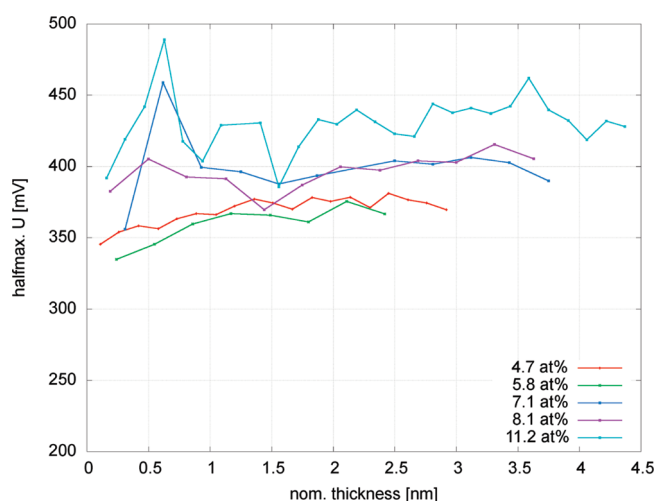
resistivity values and almost no change of resistivity as a function of the Nb concentration.

The materials library S2 shows slightly higher resistivity than S1 that increases with decreasing Nb concentration. The lowest values, close to 1×10^{-4} Ω cm, were obtained for Nb concentrations >18 at.%. Analyzing the XRD spectra of materials library S2 (Figure 3), for Nb concentrations <18 at.%, the rutile phase of TiO_2 decreases strongly and the Ti_2O suboxide is becoming predominant instead. Therefore, we assume that the lower resistivity values obtained in the presence of the rutile phase are actually related to the more metallic character of the films present underneath the TiO_2 layer formed at the surface and they are not a property of the rutile phase itself. From the XRD patterns, the rutile phase seemed to decrease together with the metallic phase. Probably during the 4-point measurements, the needle-type probes poke through the TiO_2 rutile layer from the surface, and the measured resistance is, therefore, related to the presence of the metallic phase underneath. For Nb concentrations <16 at.%, the main phase is Ti_2O leading to a slightly higher resistivity.

XPS. Figure 1 shows schematically the part of the wafer applied in the XPS analysis. Pt stripes have a nominal thickness gradient from 5 to 0 nm. The highlighted area represents the part
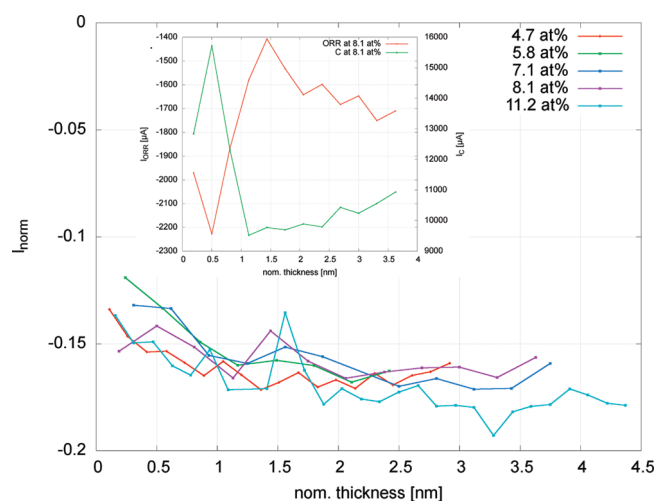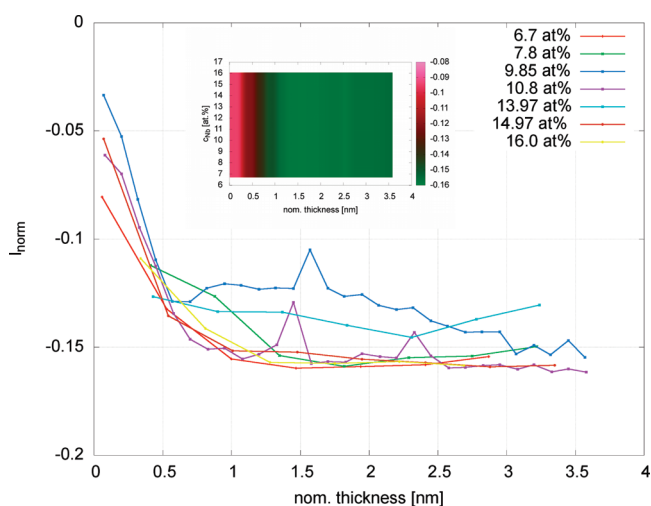
Figure 6. Line scans on S1 showing normalized ORR currents. Inset: non-normalized ORR currents and capacitive currents.
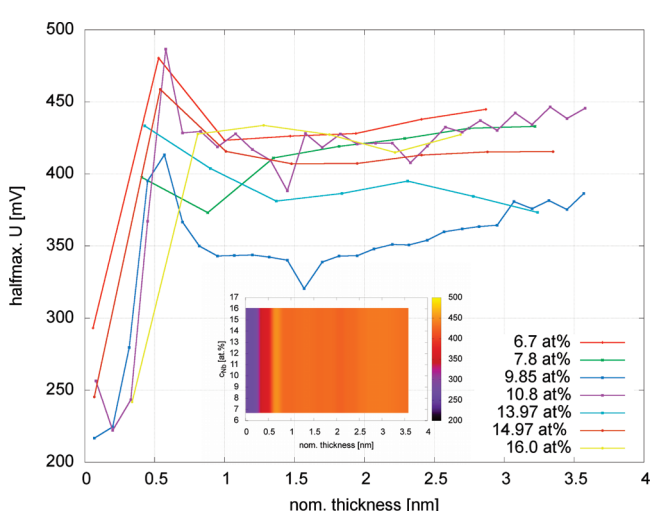

Figure 8. Normalized ORR currents S1. Inset: interpolated 3D mapping showing the trend.

Figure 7. Line scans on S1 showing the potentials at half-maximum currents.

Figure 9. Half-maximum potentials of the oxygen reduction current for the library S2. Inset: interpolated 3D mapping showing the trends.

from the wafer that was used in the XPS investigation. An elemental composition profile analysis based on survey spectra for S2, Line 8 as a function of Pt nominal thickness, is shown in Figure 5.

The different symbols represent the experimental atomic concentration percentage for Pt 4d, Ti 2p, Nb 3d, O 1s, and C 1s as indicated. Solid lines represent fits using a Boltzmann-type function. The profiles show a significant change around a nominal thickness of 1.38 nm Pt. The decrease in the atomic concentration of Pt and the increase in the Ti, O, and Nb atomic concentrations can be related to either a sudden decrease in the Pt film thickness or to the loss of the Pt film continuity. Moreover, the carbon profile presents a particular feature. Against expectations, its concentration decreases with decreasing Pt. To find a possible source of carbon contamination, the sample was heated in situ at 473 K (200 °C) for 1 h in high vacuum. These conditions should be sufficient to remove any possible adsorbed carbon species. However, the measurements performed after the heating treatment showed similar results to the previous ones. A possible reason for this might be that the

Nb-TiO₂ surface was already contaminated with carbon prior to the Pt deposition. Since the carbon contaminations are entrapped between Pt and substrate, they are not removed by heat treatments.

Electrochemical Activity and Catalytic Activity for Oxygen Reduction. Figure 6 shows the normalized ORR currents obtained during several line scans of the SDC on the materials library S1. These currents are very uniform across the materials library and show only a decrease of about 20% at nominal thicknesses of <1 nm. Figure 7 visualizes the half-maximum potentials during the same line scans on this materials library and shows also only a very small decrease in potentials. Especially, the lines with a higher Nb content and, thus, slightly higher conductivity do not show even a small decrease. The surface-normalized activity of the Pt on S1 is thus mostly independent of the substrate composition and even the Pt film thickness.

The inset in Figure 6 displays the non-normalized ORR currents as well as the capacitance in one line. It demonstrates a huge increase in reduction currents as well as capacitive currents below a Pt thickness of ∼1.1 nm. Obviously, at

thicknesses larger than ∼1 nm, the Pt film is continuous and thick enough that the top layer is not significantly influenced by the underlying support material. When the Pt film thickness is smaller than a critical thickness, it breaks up into isolated islands. Concomitantly, the active surface area increases, leading to higher capacities and reduction currents. The electrical resistance of the Pt film is expected to increase significantly at this point; however, if the substrate has a comparatively high conductivity, it is able to electrically connect the Pt islands and compensate for the loss of the continuity in the Pt film.

If these assumptions are correct, one should expect a strong influence of the substrate conductivity on the measured parameters in the area of dispersed Pt clusters, i.e., at nominal film thicknesses below about 1.1 nm Pt. Therefore, the same screening was performed using the materials library S2, which shows lower substrate conductivity but otherwise very similar properties. Figure 8 shows several line scans from S2 and visualizes the normalized oxygen reduction current at 450 mV. It can clearly be seen that it also changes very little along the lines until the nominal thickness is below about 1 nm. At lower thicknesses than 0.6 nm, the activity drops abruptly.

In Figure 9, the half-maximum potentials of the ORR are plotted along several lines vs the nominal thickness. These potentials also change very little for thicknesses >1 nm. For thinner films, the potentials initially rise significantly until a Pt film thickness of ∼0.6 nm and drop sharply at even smaller film thickness. This increase is comparatively small; however, it is significant since it is observed for all Pt stripes. Both Figures 8 and 9 show clearly that the normalized ORR currents as well as the potentials at half-maximum currents are independent of the substrate composition and the thickness for thicknesses >1.2 nm. For all measured Pt stripes, the drop in current and potential occurs at roughly the same nominal Pt film thickness. Additionally, the potentials feature a slight increase before the sharp drop.

A likely explanation is that the Pt film is continuous for thicknesses larger than 1.2 nm and fragments into isolated Pt islands below that thickness, therefore losing its continuity just as seen above for S1. However, S2 consists of oxide layers with a lower conductivity, and hence, the substrate is not able to electrically connect the isolated Pt islands as efficiently as in case of S1. As the nominal thickness decreases, the distances between the dispersed Pt clusters increase, which is accompanied with a potential drop along this distance and, thus, a decrease in the effective reduction potential. Additionally, a decrease in the active surface area may be expected once the nominal thickness gets below a certain value leading to further activity loss.

These observations are in agreement with our expectations. A more conductive substrate layer can connect isolated Pt islands more effectively, preventing a pronounced loss in the catalytic activity for the ORR. The intermediate increase in the potentials at half-maximum ORR currents is difficult to interpret, but one possibility may be seen in the presence of Pt particles with size-to-surface ratio favoring the ORR activity.

The fact that there are only little differences in the activity across the materials libraries seems unexpected at first, but from our results, we conclude that the influence of the substrate on the Pt activity for the thick parts of the Pt films is negligible, and differences can be expected only in the thin parts. In this regime, we regard the substrate conductivity as having the most important impact on the measured catalytic activity for the ORR.

■ CONCLUSION

The catalytic activity for the reduction of oxygen at thin Pt films sputtered on oxidized Ti/Nb surfaces is not significantly influenced by the substrate as long as the Pt film has a nominal thickness of >1 nm. Below this threshold, the activity of the catalyst drops sharply. At such small thicknesses, the observed activity is significantly influenced by the substrate, and we assume that its conductivity plays a decisive role. XPS measurements suggest the presence of isolated Pt islands at ∼1.3 nm, which is in agreement with the values derived from the SDC measurements.

Our findings are supported by a recent study of Hayden et al.[29,30] on Pt supported by titanium oxide and carbon supports, who found a critical threshold of 0.65 nm below which the activity of TiO-supported Pt dropped abruptly but not that of carbon-based Pt. The proposed method for the preparation of Pt films supported on different material libraries as well as the developed fast screening technique using a SDC is seen as a promising concept for applied catalyst research. Further plans encompass a variety of different substrates as well as Pt films with a smaller thickness gradient for increased resolution measurements.

■ AUTHOR INFORMATION

Corresponding Author

*E-mail: wolfgang.schuhmann@rub.de. Fax: +49-234-3214683. Internet: www.rub.de/elan.

Present Addresses

[⊥]Instituto de Física del Sur (UNS-CONICET), Av. Alem 1253, 8000 Bahía Blanca, Argentina.

■ REFERENCES

(1) Potyrailo, R. A.; Mirsky, V. M. *Chem. Rev.* **2008**, *108*, 770–813.

(2) Takeuchi, I.; Lauterbach, J.; Fasolka, M. *J. Mater. Today* **2005**, *8*, 18–26.

(3) Xiang, X.-D. *Combinatorial materials synthesis*; Marcel Dekker: New York, 2003.

(4) Ludwig, A.; Zarnetta, R.; Hamann, S.; Savan, A.; Thienhaus, S. *Int. J. Mater. Res.* **2008**, *99*, 1144–1149.

(5) Zarnetta, R.; Takahashi, R.; Young, M. L.; Savan, A.; Furuya, Y.; Thienhaus, S.; Maass, B.; Rahim, M.; Frenzel, J.; Brunken, H.; Chu, Y. S.; Srivastava, V.; James, R. D.; Takeuchi, I.; Eggeler, G.; Ludwig, A. *Adv. Funct. Mater.* **2010**, *20*, 1917–1923.

(6) Koinuma, H.; Takeuchi, I. *Nat. Mater.* **2004**, *3*, 429–438.

(7) Prochaska, M.; Jin, J.; Rochefort, D.; Zhuang, L.; DiSalvo, F. J.; Abruña, H. D.; van Dover, R. B. *Rev. Sci. Instrum.* **2006**, *77*, 54104.

(8) Jin, J.; Prochaska, M.; Rochefort, D.; Kim, D.; Zhuang, L.; Disalvo, F.; Vandover, R.; Abruña, H. D. *Appl. Surf. Sci.* **2007**, *254*, 653–661.

(9) Woodhouse, M.; Herman, G. S.; Parkinson, B. A. *Chem. Mater.* **2005**, *17*, 4318–4324.

(10) Woodhouse, M.; Parkinson, B. A. *Chem. Mater.* **2008**, *20*, 2495–2502.

(11) Hassel, A. W.; Lohrengel, M. M. *Electrochim. Acta* **1997**, *42*, 3327–3333.

(12) Lohrengel, M. M.; Moehring, A.; Pilaski, M. *Electrochim. Acta* **2001**, *47*, 137–141.

(13) Williams, C. G.; Edwards, M. A.; Colley, A. L.; MacPherson, J. V.; Unwin, P. R. *Anal. Chem.* **2009**, *81*, 2486–2495.

(14) Mardare, A. I.; Savan, A.; Ludwig, A.; Wieck, A. D.; Hassel, A. W. *Corros. Sci.* **2009**, *51*, 1519–1527.

(15) Mardare, A. I.; Savan, A.; Ludwig, A.; Wieck, A. D.; Hassel, A. W. *Electrochim. Acta* **2009**, *54*, 5973–5980.

(16) Mardare, A. I.; Ludwig, A.; Savan, A.; Wieck, A. D.; Hassel, A. W. *Electrochim. Acta* **2009**, *54*, 5171–5178.

(17) Fernández, J. L.; Bard, A. J. *Anal. Chem.* **2003**, *75*, 2967–2974.

(18) Fernández, J. L.; Hurth, C.; Bard, A. J. *J. Phys. Chem. B* **2005**, *109*, 9532–9539.

(19) Sanchez-Sanchez, C. M.; Bard, A. J. *Anal. Chem.* **2009**, *81*, 8094–8100.

(20) Sanchez-Sanchez, C. M.; Rodiriguez-Lopez, J.; Bard, A. J. *Anal. Chem.* **2008**, *80*, 3254–3260.

(21) Fernández, J. L.; Walsh, D. A.; Bard, A. J. *J. Am. Chem. Soc.* **2005**, *127*, 357–365.

(22) Eckhard, K.; Schuhmann, W. *Electrochim. Acta* **2007**, *53*, 1164–1169.

(23) Burch, R. *Chem. Ind.* **1988**, *31*, 347–372.

(24) Roen, L. M.; Paik, C. H.; Jarvi, T. D. *Electrochem. Solid-State Lett.* **2004**, *7*, A19–A22.

(25) Tian, J.; Sun, G.; Cai, M.; Mao, Q.; Xin, Q. *J. Electrochem. Soc.* **2008**, *155*, B187–B193.

(26) Drew, K.; GirishKumar, G.; Vinodgopal, K.; Kamat, P. V. *J. Phys. Chem. B* **2005**, *109*, 11851–11857.

(27) Kinoshita, K. *J. Electrochem. Soc.* **1990**, *137*, 845–848.

(28) Guerin, S.; Hayden, B. E.; Pletcher, D.; Rendall, M. E.; Suchsland, J.-P. *J. Comb. Chem.* **2006**, *8*, 679–686.

(29) Hayden, B. E.; Pletcher, D.; Suchsland, J.-P.; Williams, L. J. *Phys. Chem. Chem. Phys.* **2009**, *11*, 1564–1570.

(30) Hayden, B. E.; Pletcher, D.; Suchsland, J.-P.; Williams, L. J. *Phys. Chem. Chem. Phys.* **2009**, *11*, 9141–9148.

(31) Thienhaus, S.; Zamponi, C.; Rumpf, H.; Hattrick-Simpers, J.; Takeuchi, I.; Ludwig, A. *Mater. Res. Soc. Symp. Proc.* **2006**, *894*, 197–203.

(32) Mardare, A. I.; Wieck, A. D.; Hassel, A. W. *Electrochim. Acta* **2007**, *52*, 7865–7869.

(33) Hassel, A. W.; Fushimi, K.; Seo, M. *Electrochem. Commun.* **1999**, *1*, 180–183.

(34) Brown, A. R. G.; Clark, D.; Eastabrook, J.; Jepson, K. S. *Nature* **1964**, *201*, 914–915.

(35) Lee, C. M.; Ju, C. P.; Lin, J. H. C. *J. Oral Rehabil.* **2002**, *29*, 314–322.

(36) Maaza, M.; Sella, C.; Ambroise, J. P.; Kaabouchi, M.; Miloche, M.; Wehling, F.; Groos, M. *J. Appl. Crystallogr.* **1993**, *26*, 334–342.

(37) Jiang, H.; Hirohasi, M.; Imanari, H.; Lu, Y. *Scr. Mater.* **2001**, *45*, 253–259.

(38) Bartholomew, R. F.; Frankl, D. R. *Phys. Rev.* **1969**, *187*, 828–833.